

# Performance of asymmetric supercapacitor fabricated with perovskite-type $\text{Sr}^{2+}$ -incorporated $\text{LaMnO}_3$ ( $\text{La}_{0.7}\text{Sr}_{0.3}\text{MnO}_3$ ) nanostructures in neutral 1M $\text{Na}_2\text{SO}_4$ aqueous electrolyte

Atanu Roy<sup>1</sup> | Francisco Enrique Cancino-Gordillo<sup>2</sup>  | Samik Saha<sup>1,3</sup> |  
Umapada Pal<sup>2</sup> | Sachindranath Das<sup>1</sup> 

<sup>1</sup>Department of Instrumentation Science, Jadavpur University, Kolkata, India

<sup>2</sup>Instituto de Física, Benemérita Universidad Autónoma de Puebla, Puebla, Mexico

<sup>3</sup>Department of Physics, Jadavpur University, Kolkata, India

## Correspondence

Sachindranath Das, Department of Instrumentation Science, Jadavpur University, Kolkata 700032, India.  
Email: sachindas15@gmail.com; sachindran.das@jadavpuruniversity.in

Umapada Pal, Instituto de Física, Benemérita Universidad Autónoma de Puebla, Apdo. Postal J-48, Puebla 72570, Mexico.

Email: upal@ifuap.buap.mx

## Funding information

Consejo Nacional de Ciencia y Tecnología, Grant/Award Number: CB-A1-S-26720; Council of Scientific and Industrial Research, India, Grant/Award Number: 09/096(0898)/2017-EMR-I; RUSA 2.0, Jadavpur University, Grant/Award Number: R-11/281/19; Science and Engineering Research Board, Grant/Award Number: CRG/2019/001575

## Summary

Strontium (Sr) incorporated  $\text{LaMnO}_3$  ( $\text{La}_{0.7}\text{Sr}_{0.3}\text{MnO}_3$ ) nanoparticles have been synthesized by ball-milling-assisted solid-state reaction to study their performance as electrode material for energy storage applications. The  $\text{La}_{0.7}\text{Sr}_{0.3}\text{MnO}_3$  nanoparticles exhibit superior electrochemical performance in neutral aqueous electrolyte (1 M  $\text{Na}_2\text{SO}_4$ ) in comparison to  $\text{LaMnO}_3$  and  $\text{SrMnO}_3$  nanoparticles. This neutral electrolyte provides relatively higher ionic conductivity and viscosity compared to the ionic liquids and a wider potential window compared to the alkaline electrolytes. Electrochemical study of the electrodes prepared using  $\text{La}_{0.7}\text{Sr}_{0.3}\text{MnO}_3$  nanoparticles reveals pseudocapacitive behaviors with fast reversible Faradaic charge storage, which plays a key role in charge storage. The composite materials exhibit highest specific capacitance of  $393.5 \text{ F g}^{-1}$  at a scan rate of  $2 \text{ mV s}^{-1}$ . Asymmetric supercapacitors fabricated using  $\text{La}_{0.7}\text{Sr}_{0.3}\text{MnO}_3$  nanoparticle and activated carbon operates over a wide potential window of 1.8 V, and it reveals high specific capacitance ( $197 \text{ F g}^{-1}$ ) as well as high capacitive retention (87%) even after 4000 charge–discharge cycles.

## KEYWORDS

nanostructured electrode, neutral electrolyte, perovskite, pseudocapacitance, supercapacitor

## 1 | INTRODUCTION

Energy is the foremost concern of the present day society because of the exponential rise in global energy demand and rapid depletion of fossil fuel reserve. In order to mitigate the energy crisis as well as pollution issues associated with fossil fuel burning, continuous innovation in the energy sector is essential. Current processes involved

in energy generation, delivery, and storage need tremendous upgradation to meet the global challenge for the generation of clean and inexpensive energy. Solar radiation, ocean tide, wind, and biofuels have been envisioned as some of the most attractive renewable energy resources which can provide clean energy at a reasonable cost. However, due to the intermittent nature of these renewable energy sources, not only the generation but

also the storage of generated energy needs substantial attention. In fact, several energy storage devices such as supercapacitors, batteries, and fuel cells of enhanced performance have been developed in the past two decades, although they remained insufficient to fulfill the global energy demand.

A supercapacitor or electrochemical capacitor or ultracapacitor is a class of energy storage device, which received a tremendous attention in recent time because of its rapid charge–discharge rates, high power density, and relatively large cycle life compared to Li-ion battery.<sup>1,2</sup> Supercapacitors are broadly categorized into two classes depending upon their charge storage mechanism: (a) electric double-layer capacitors (EDLCs) and (b) pseudocapacitors. In EDLCs, a double layer is formed at the electrode/electrolyte interface. Mainly, carbonaceous materials and their derivatives belong to this category.<sup>3–6</sup> On the other hand, a pseudocapacitor stores charge via rapid faradaic reaction within the electrode material. Transition metal oxides (eg, RuO<sub>2</sub>, MnO<sub>2</sub>, NiO, Co<sub>2</sub>O<sub>3</sub>, etc.) and conducting polymers (eg, Polyaniline, poly-pyrrole, etc.) follow this mechanism.<sup>7–14</sup>

Among the metal oxides, ABO<sub>3</sub>-type perovskite materials have gained ample research interest because of their excellent electronic structure, outstanding thermal stability, and exceptional ionic conductivity. Because of high electron-ion double conductivities and structural stability at elevated temperatures, metal oxide perovskite materials are the automatic choice as electrode materials in solid oxide fuel cells.<sup>15–17</sup> High ionic and electronic conductivity enable them to be efficient electrode materials for supercapacitors. ABO<sub>3</sub>-type perovskites also possess the ability of rapid faradaic redox reaction at their surface, which enables them to be potential candidates for supercapacitor electrodes.<sup>18,19</sup> Moreover, ABO<sub>3</sub>-type perovskites with lanthanide or alkaline-earth elements as A and transition metals as B atom have intrinsic oxygen vacancies, which enable them to act as electrode material for supercapacitors via faradic redox reaction. Pseudocapacitive charge storage mechanism involves mainly three processes: (a) adsorption of electrolyte ions to form a monolayer over metal or metal oxide surface, known as underpotential deposition, (b) fast reversible redox reaction at the electrode surface, and (c) fast intercalation/deintercalation of electrolyte ions into bulk electrode.<sup>20</sup> LaMnO<sub>3+δ</sub> is a popular metal oxide of perovskite structure, which can form with substoichiometric as well as superstoichiometric oxygen content, that is,  $-0.25 \leq \delta \leq 0.25$ .<sup>21–23</sup> Moreover, it is well-known that a partial replacement of A site in LaMnO<sub>3</sub> with Sr<sup>2+</sup> or Ca<sup>2+</sup> (lower valence cation) generates holes in B site. To maintain the charge neutrality, Mn<sup>3+</sup> ions of LaMnO<sub>3</sub> lattice oxidize to form Mn<sup>4+</sup> ions. This

oxidization enhances the electrical conductivity as well as ion diffusion rate, which in turn enhances the overall electrochemical performance of the material. LaMnO<sub>3</sub> is the most commonly used perovskite electrode material for supercapacitors. It has been observed that substituting at A site (position of La) as well as B sites (position of Mn) with suitable element enhances the electrochemical performance of LaMnO<sub>3</sub>. As has been reported by Wang et al, the specific capacitance of LaMnO<sub>3</sub> increases from 187 to 198 F g<sup>-1</sup> on Sr doping. At the same time, the cyclic stability of the supercapacitors made of LaMnO<sub>3</sub> increases from 40% to 80% after 1000 cycles.<sup>24</sup> Cao et al have also seen an enhancement of specific capacitance of LaMnO<sub>3</sub>-based supercapacitors from 100 to 464.5 F g<sup>-1</sup> by incorporating Sr and Cu at A and B sites, respectively.<sup>16</sup> However, both the above mentioned works as well as most of the previously reported works have utilized either toxic nonaqueous electrolyte or aqueous alkaline electrolytes (NaOH or KOH) of high concentrations. Replacement of these electrolytes with neutral and commonly available aqueous electrolytes such as Na<sub>2</sub>SO<sub>4</sub> solution will improve the potential window as the hydrogen or oxygen evolution potential will shift toward higher potential due to the low concentration of H<sup>+</sup> and OH<sup>-</sup> ions in the solution.<sup>25</sup> Neutral aqueous electrolytes are less corrosive compared to high concentration acidic or basic electrolytes, providing relatively long life for the supercapacitors.<sup>26</sup> Aqueous Na<sub>2</sub>SO<sub>4</sub> electrolyte provides high power and wide operational temperature over nonaqueous electrolytes and wide potential window over KOH electrolyte.<sup>27–30</sup> Moreover, the Na<sub>2</sub>SO<sub>4</sub> electrolyte provides better ionic conductivity and low viscosity compared to the ionic liquid electrolytes.<sup>30</sup> The natural abundance and low cost of Na<sub>2</sub>SO<sub>4</sub> may act as an advantageous feature for the commercialization of the supercapacitor.

In the present work, we synthesized La<sub>0.7</sub>Sr<sub>0.3</sub>MnO<sub>3</sub> nanoparticles along with LaMnO<sub>3</sub> and SrMnO<sub>3</sub> via ball-milling and analyzed their structural and electrochemical properties in an aqueous 1 M Na<sub>2</sub>SO<sub>4</sub> electrolyte. The potential of the nanoparticles as supercapacitor electrode material has been studied by fabricating asymmetric supercapacitors (ASC), which provided a wide potential window with high specific capacitance and capacitive retention.

## 2 | EXPERIMENTAL SECTION

### 2.1 | Chemicals

Precursors and reactants such as manganese nitrate tetrahydrate (Mn[NO<sub>3</sub>]<sub>2</sub>·4H<sub>2</sub>O, >97.0%), lanthanum nitrate hexahydrate (La[NO<sub>3</sub>]<sub>3</sub>·6H<sub>2</sub>O, 99.99%), strontium nitrate (Sr[NO<sub>3</sub>]<sub>2</sub>, 99 + %), and acetylacetone (C<sub>5</sub>H<sub>8</sub>O<sub>2</sub>,

>99.5%) were acquired from Sigma-Aldrich, Mexico. Sodium hydroxide (NaOH, 98.15%) and sodium chloride (NaCl, >99%) were purchased from J.T. Baker, and Omnicom, Mexico, respectively. Deionized (DI) water from a Millipore system ( $\rho >18.2 \text{ M } \Omega \text{ cm}$ ) was utilized for washing (samples and glasswares) purpose.

## 2.2 | Synthesis

Metal acetylacetonate complexes ( $\text{Mn}(\text{acac})_2$ ,  $\text{La}(\text{acac})_3$  and  $\text{Sr}(\text{acac})_2$ ) were initially synthesized through coprecipitation method.<sup>31</sup> For the synthesis of  $\text{Mn}(\text{acac})_2$ , sodium acetylacetonate solution (solution 1), which was used as a precipitating agent, was prepared by drop-wise addition of 15 mL acetylacetone to 60 mL NaOH solution (8.7 mM) at 50°C under magnetic stirring. A precursor solution (solution 2) of Mn was then prepared separately by dissolving 48.49 mM of manganese nitrate tetrahydrate in 50 mL of DI water. After that, the hot sodium acetylacetonate solution (solution 1) was slowly added to the Mn precursor solution (solution 2) and kept at 50°C for 30 minutes under magnetic stirring. After cooling, the pale-yellow precipitate of manganese acetylacetonate ( $\text{Mn}(\text{acac})_2$ ) was separated by vacuum filtering in a Büchner funnel, washed four times with DI water, and vacuum dried for 12 hours. The same procedure was followed to synthesize the  $\text{La}(\text{acac})_3$  and  $\text{Sr}(\text{acac})_2$  precursors. Colors of the latter two precursors were white and pearl-white, respectively.

$\text{La}_{1-x}\text{Sr}_x\text{MnO}_3$  nanoparticles were then prepared by ball-milling-assisted solid-state reaction of the metal acetylacetonate precursors in presence of sodium chloride, which acted as a dispersing agent. For the synthesis of  $\text{La}_{0.7}\text{Sr}_{0.3}\text{MnO}_3$ , 0.5783 g of  $\text{Mn}(\text{acac})_2$ , 0.6863 g of  $\text{La}(\text{acac})_3$ , and 0.1823 g of  $\text{Sr}(\text{acac})_2$  were mixed with 7.234 g of NaCl. Then, the mixture was placed inside a 100 mL agate milling jar filled with 32 agate grinding balls (10 mm diameter) and placed in a planetary ball-milling (PQ-N2 Gear Drive 4) station. The milling was performed at 200 rpm for 24 hours. The obtained fine powder was then transferred to an alumina crucible and air-annealed inside a tubular (Carbolite) furnace at 700°C (increased at 5°C/min rate) for 8 hours. To remove NaCl, the obtained product was washed repeatedly with warm (70°C) DI water. Finally, the sample was collected by centrifugation and dried at 70°C for 5 hours. To induce crystallization in the formed nanostructures, the powder sample was further air-annealed at 850°C (at 5°C/min heating rate) for 12 hours. The same procedure was followed for the fabrication of  $\text{SrMnO}_3$  and  $\text{LaMnO}_3$  nanostructures.

## 2.3 | Characterization

To analyze the crystallinity and phase structure of the synthesized nanostructures, powder X-ray diffraction (XRD) was performed using a Bruker D8 diffractometer, utilizing  $\text{CuK}\alpha$  ( $\lambda = 1.5406 \text{ \AA}$ ) radiation. The spectra were recorded at 0.02°/step with a scan rate of 0.2 second/step in 20 to 80° span. Chemical composition and morphology of the nanostructures were analyzed in a JEOL JSM-7800F field-emission scanning electron microscope (FE-SEM) attached with an Oxford analytical system.

## 2.4 | Electrode fabrication

To fabricate electrodes, a gel was first prepared by mixing the sample material ( $\text{La}_{1-x}\text{Sr}_x\text{MnO}_3$ ,  $\text{SrMnO}_3$ , and  $\text{LaMnO}_3$ ), activated carbon, and polyvinylidene fluoride (PVDF) (mass ratio 85:10:5) in *N*-methyl-2-pyrrolidone (NMP) under ultrasonic agitation. The working electrodes were then prepared by drop-casting the active material gel on Teflon-coated carbon rods and then dried overnight at 60°C under vacuum.

## 2.5 | Device fabrication

The ASCs were fabricated by coating the aforesaid gel on one side of a stainless steel current collector (3 cm × 4 cm) which served as a positive electrode and a gel of activated carbon on one side of another stainless steel current collector which served as a negative electrode. These two electrodes were assembled along with a separator (Whatman filter paper, pore diameter 25 μm). The filter paper was soaked with 1 M  $\text{Na}_2\text{SO}_4$  electrolyte solution. The masses of the active materials were selected by charge balancing theory ( $Q_+ = Q_-$ ). According to this theory, the mass ratio of two electrodes should be:

$$\frac{m_+}{m_-} = \frac{C_- \times \Delta V_-}{C_+ \times \Delta V_+} \quad (1)$$

where,  $m$ ,  $C$ , and  $\Delta V$  refers to the masses, specific capacitance ( $\text{F g}^{-1}$ ), and the potential window ( $V$ ) of respective electrode materials.<sup>32,33</sup>

## 2.6 | Electrochemical measurements

A conventional three-electrode set up was utilized to study the electrochemical performance of the electrode materials with Ag/AgCl (saturated KCl) and Pt plate (1 cm × 1 cm) as the reference electrode and counter

electrode, respectively, and 1 M Na<sub>2</sub>SO<sub>4</sub> aqueous solution as the electrolyte. An electrochemical analyzer (CS313, CorrTest, China) was used to measure the cyclic voltammetry (CV), galvanostatic charge–discharge (GCD), and electrochemical impedance spectroscopy (EIS). The values of specific capacitance were calculated from CV curves using Equation (2):

$$C_s = \frac{1}{2mv(V_f - V_i)} \int_{V_i}^{V_f} I(V)dV \quad (2)$$

where  $C_s$  is the capacitance per unit mass (F g<sup>-1</sup>),  $\int_{V_i}^{V_f} I(V)dV$  refers total area enclosed by the CV curve,  $m$  refers to the mass of the active electrode (g),  $v$  is the potential scan rate (V s<sup>-1</sup>), and  $(V_f - V_i)$  is the working window (V).<sup>33–35</sup> GCD curves were also used to compute the same, using the Equation (3):

$$C_s = \frac{I}{m \times \frac{dV}{dt}} \quad (3)$$

where  $I/m$  refers to the discharge current density (A g<sup>-1</sup>) and  $\frac{dV}{dt}$  refers to the average slope of the discharge curve.

All three electrochemical measurements, that is, CV, GCD, and EIS were also performed on the fabricated ASC devices. Specific energy and specific power of the devices were estimated from the GCD data. Energy density ( $E$ ) (Wh kg<sup>-1</sup>) and power density ( $P$ )

(W kg<sup>-1</sup>) of the ASC devices were obtained using the equations:

$$E = \frac{1}{2} \left[ \frac{C_s (V_f - V_i)^2}{3.6} \right] \quad (4)$$

and

$$P = \frac{3600 \times E}{\Delta t} \quad (5)$$

where  $\Delta t$  is the discharge time.<sup>36</sup>

### 3 | RESULTS AND DISCUSSION

X-ray diffraction (XRD) patterns of the nanoparticles were recorded to study their structure, phase, and phase purity (Figure 1). As can be noticed in Figure 1A, diffraction peaks of the as-prepared SrMnO<sub>3</sub> and LaMnO<sub>3</sub> nanoparticles correspond fully to their hexagonal (JCPDF #04-015-4143) and rhombohedral (JCPDF #04-012-5560) phase, respectively. No peak associated with impurity or undesired phase was observed. All the diffraction peaks of the La<sub>0.7</sub>Sr<sub>0.3</sub>MnO<sub>3</sub> sample also corresponded to its rhombohedral (JCPDF #00-056-0616) phase. XRD study confirms that all the three compounds have ABO<sub>3</sub>-type perovskite structures. With the incorporation of Sr<sup>2+</sup> in LaMnO<sub>3</sub>, the intensity of the diffraction peaks decreased, probably due to the partial replacement of La<sup>3+</sup> ions of

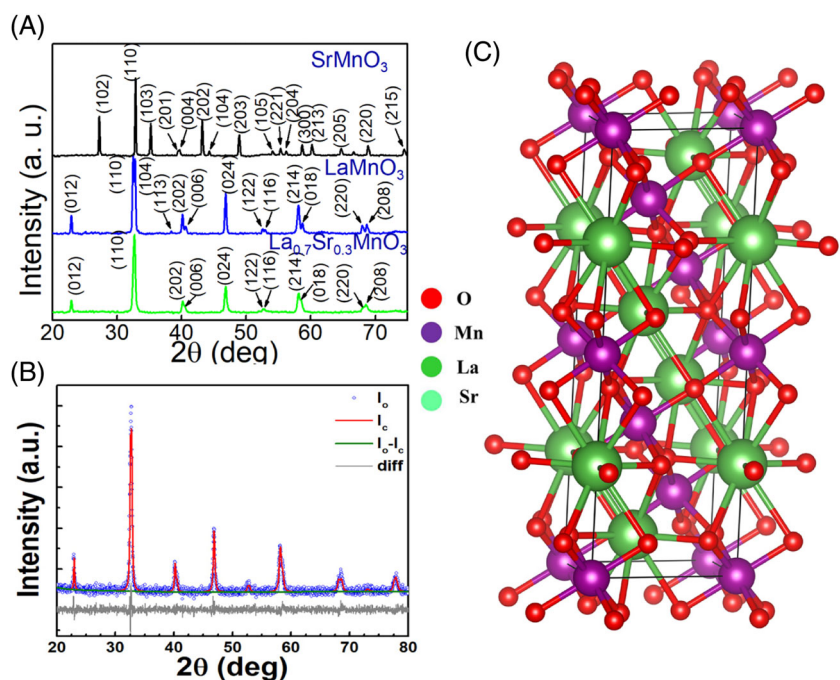


FIGURE 1 A, The XRD curves of SrMnO<sub>3</sub>, LaMnO<sub>3</sub>, and La<sub>0.7</sub>Sr<sub>0.3</sub>MnO<sub>3</sub>; B, typical Rietveld analysis output profiles of La<sub>0.7</sub>Sr<sub>0.3</sub>MnO<sub>3</sub> nanostructures; and C, schematic atomic model of La<sub>0.7</sub>Sr<sub>0.3</sub>MnO<sub>3</sub> [Colour figure can be viewed at wileyonlinelibrary.com]

A-sites by  $\text{Sr}^{2+}$  ions. Microstructural properties of the  $\text{La}_{0.7}\text{Sr}_{0.3}\text{MnO}_3$  nanostructures were further investigated through Rietveld refinement, using GSAS-II (version 4379) data analysis software.<sup>37</sup> The experimental and refined XRD data of  $\text{La}_{0.7}\text{Sr}_{0.3}\text{MnO}_3$  are shown in Figure 1B. Rietveld refinement also confirms the rhombohedral structure of  $\text{La}_{0.7}\text{Sr}_{0.3}\text{MnO}_3$  with R-3c:H space group symmetry and lattice parameters  $a = b = 5.51 \text{ \AA}$  and  $c = 13.37 \text{ \AA}$ . Marquardt least-square technique was used to minimize the difference between experimental and refined diffraction pattern. Microstrain and lattice parameters of the crystallites were calculated using the Pseudo-Voigt (PV) function. The quality of refinement and reliability of the extracted parameters were guaranteed by measuring the goodness of fitting (GoF), which is the ratio of weighted residual error ( $R_{\text{wp}}$ ) and expected error ( $R_{\text{ex}}$ ). The goodness of fitting (GoF) value

was 1.06, which is close to unity and implies a good fitting of the data. The refined output was used to construct the unit cell, using VESTA software package, as shown in Figure 1C. Typical FE-SEM micrographs of the  $\text{LaMnO}_3$ ,  $\text{SrMnO}_3$ , and  $\text{La}_{0.7}\text{Sr}_{0.3}\text{MnO}_3$  nanoparticles are presented in Figure 2A-C. As can be seen, the  $\text{SrMnO}_3$  sample consists of quasi-spherical particles of 110 to 500 nm (ca.  $256 \pm 87 \text{ nm}$ ) sizes, and the  $\text{LaMnO}_3$  sample contains agglomerated quasi-spherical particles of 35 to 180 nm sizes (ca.  $89.6 \pm 26 \text{ nm}$ ). Incorporation of  $\text{Sr}^{2+}$  ions in  $\text{LaMnO}_3$  through partial substitution of  $\text{La}^{3+}$  ions at A-sites causes an increment of particle size as observed in the sample  $\text{La}_{0.7}\text{Sr}_{0.3}\text{MnO}_3$  (ca. particle size  $128.7 \pm 39 \text{ nm}$ ). Incorporation of  $\text{Sr}^{2+}$  ions causes a reduction in the dispersion of  $\text{LaMnO}_3$  particles, causing the formation of an interconnected network due to their partial fusion during high-temperature annealing. Such

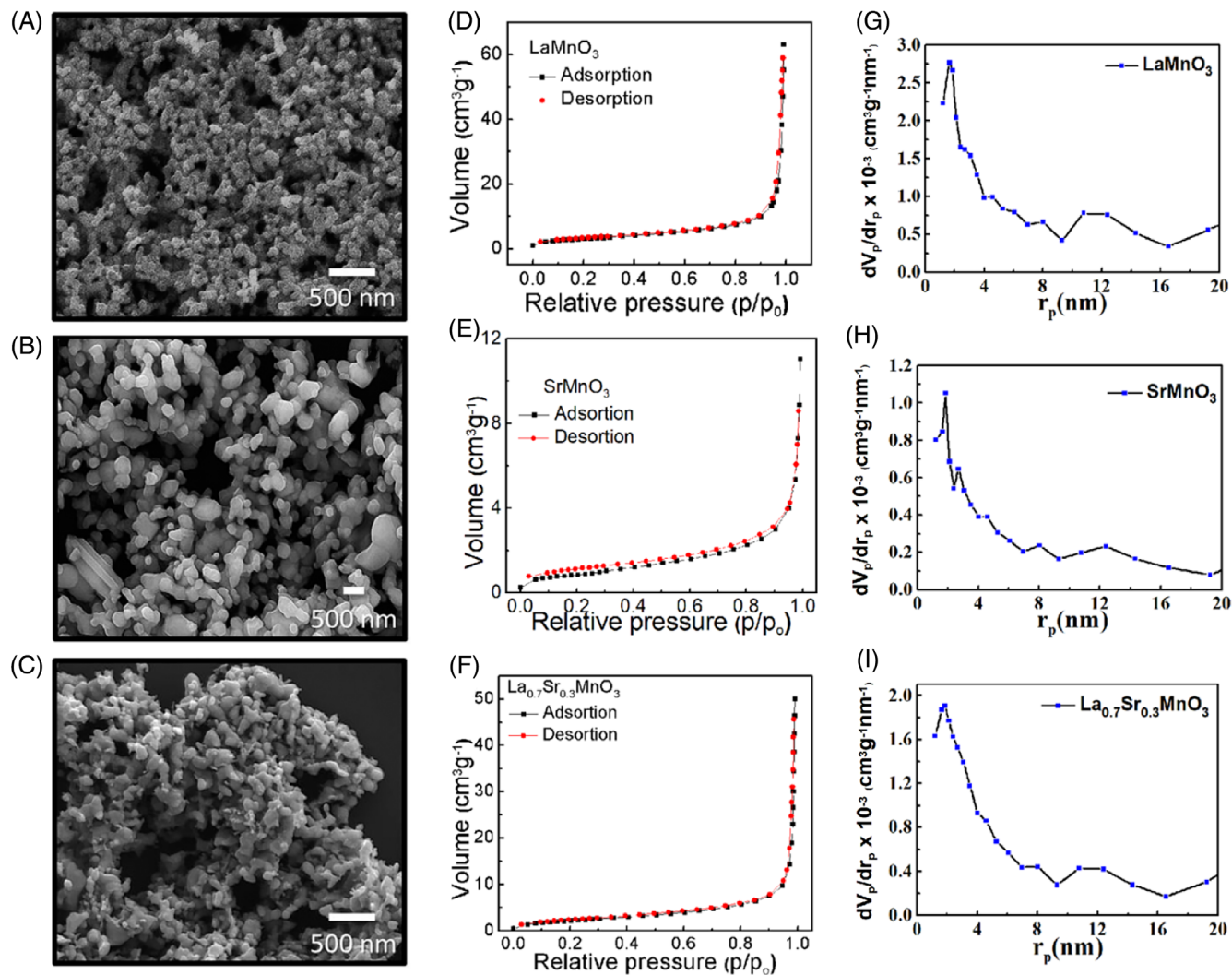


FIGURE 2 FE-SEM images (left column) A-C,  $\text{N}_2$  adsorption-desorption isotherms (middle column) D-F, and pore size distributions (right column) G-I, in the synthesized  $\text{LaMnO}_3$ ,  $\text{La}_{0.7}\text{Sr}_{0.3}\text{MnO}_3$ , and  $\text{SrMnO}_3$  nanostructures [Colour figure can be viewed at [wileyonlinelibrary.com](http://wileyonlinelibrary.com)]

interconnected nanostructures are useful for energy storage applications since they provide a larger accessible interlinked surface to the electrolyte ions.<sup>38</sup>

Nitrogen adsorption-desorption isotherms of the  $\text{LaMnO}_3$ ,  $\text{SrMnO}_3$ , and  $\text{La}_{0.7}\text{Sr}_{0.3}\text{MnO}_3$  samples recorded at 77 K are shown in Figure 2D-F. All the isotherms revealed type III characteristics, with H1-type hysteresis loop. These type III materials are found to have relatively weak adsorption-desorption interaction with nitrogen and are not very common. The H1 loops indicate well-defined cylindrical pore channels in the nanostructures which are useful for electrolyte ion transport.<sup>39,40</sup> Brunauer-Emmett-Teller (BET) analysis was used to estimate the specific surface area of the three materials. The specific surface area of  $\text{SrMnO}_3$ ,  $\text{LaMnO}_3$ , and  $\text{La}_{0.7}\text{Sr}_{0.3}\text{MnO}_3$  samples were 7.8, 10.7, and 7.9  $\text{m}^2 \text{g}^{-1}$ , respectively. BJH pore size distribution graphs of the nanostructures are presented in Figure 2G-I. Estimated average pore diameters in the  $\text{LaMnO}_3$ ,  $\text{SrMnO}_3$ , and  $\text{La}_{0.7}\text{Sr}_{0.3}\text{MnO}_3$  samples were 20.1, 32.9, and 37.8 nm, respectively. Even though the BET surface area of the  $\text{La}_{0.7}\text{Sr}_{0.3}\text{MnO}_3$  nanoparticles is relatively low, larger pores in them probably allow a large number of electrolyte ions to interact with the electrochemically active sites, resulting in a rapid redox reaction. In our previous manuscript, we have already demonstrated the TEM, EDS, XPS, and Raman spectroscopy results.<sup>41</sup> EDS of  $\text{La}_{0.7}\text{Sr}_{0.3}\text{MnO}_3$  shows the atomic % of La, Sr, Mn, O, and Na are 13.22%, 4.90%, 16.24%, 65.24%, and 0.41%, respectively. The existence of Na is also observed from the XPS measurement as well. The survey scan of the XPS spectra reveals that there is no trace of chlorine as there is no peaks at 199 and 201 eV binding energies which are designated for Cl  $2p_{3/2}$  and Cl  $2p_{1/3}$ , respectively. All the chlorine ions are removed because of the annealing at 900°C. Thus, we can conclude that there is no role of  $\text{Cl}^-$  ions in the electrochemical process. High-resolution XPS

study of  $\text{La}_{0.7}\text{Sr}_{0.3}\text{MnO}_3$  shows the presence of La  $3d_{5/2}$  and  $3d_{3/2}$  at binding energies (BE) 850.29 and 833.54 eV, respectively. High-resolution XPS study of Mn 2p confirms the presence of both  $\text{Mn}^{3+}$  and  $\text{Mn}^{4+}$  states. However, these peaks shift toward higher BEs upon the substitution of  $\text{La}^{3+}$  ions by  $\text{Sr}^{2+}$  ions. Existence of multiple cationic states of Mn is useful for the rapid redox reaction.

The CV study of the electrodes made of  $\text{SrMnO}_3$ ,  $\text{LaMnO}_3$ , and  $\text{La}_{0.7}\text{Sr}_{0.3}\text{MnO}_3$  nanoparticles was performed in 1 M  $\text{Na}_2\text{SO}_4$  aqueous electrolyte within a potential window  $-0.2$  to  $1.0$  V (vs Ag/AgCl) at different scan rates ranging from 2 to  $100 \text{ mV s}^{-1}$ . Figure 3A presents a comparison of CV data of  $\text{SrMnO}_3$ ,  $\text{LaMnO}_3$ , and  $\text{La}_{0.7}\text{Sr}_{0.3}\text{MnO}_3$  nanostructures at a fixed scan rate of  $10 \text{ mV s}^{-1}$ . Areas under these CV curves are directly proportional to the charge storage capacity of the materials. As can be noticed, the area under the CV curve of  $\text{La}_{0.7}\text{Sr}_{0.3}\text{MnO}_3$  is larger than the same of other two samples for the same scan rate, which directly implies that  $\text{La}_{0.7}\text{Sr}_{0.3}\text{MnO}_3$  possesses better charge storage capacity among the three samples. The CV curves of  $\text{La}_{0.7}\text{Sr}_{0.3}\text{MnO}_3$  recorded at different scan rates are shown in Figure 3B (CV curves of other materials are presented as Figure S1A, B in supplementary information). As can be noticed in Figure 3A, the shape of the CV curve corresponds to  $\text{SrMnO}_3$  is almost rectangular. But, the CV curve of  $\text{LaMnO}_3$  shows a deviation from the rectangular shape which indicates the pseudocapacitive mechanism dominates in charge storage. The highest specific capacitance obtained for  $\text{La}_{0.7}\text{Sr}_{0.3}\text{MnO}_3$  is  $393.5 \text{ F g}^{-1}$ , which is higher than the specific capacitance corresponds to  $\text{SrMnO}_3$  ( $54.2 \text{ F g}^{-1}$ ) and  $\text{LaMnO}_3$  electrodes ( $268.8 \text{ F g}^{-1}$ ). The variations of specific capacitance with scan rate for all three materials are presented in Figure 3C. At lower scan rates, the electrolyte ions get sufficient time to interact with the electrochemically

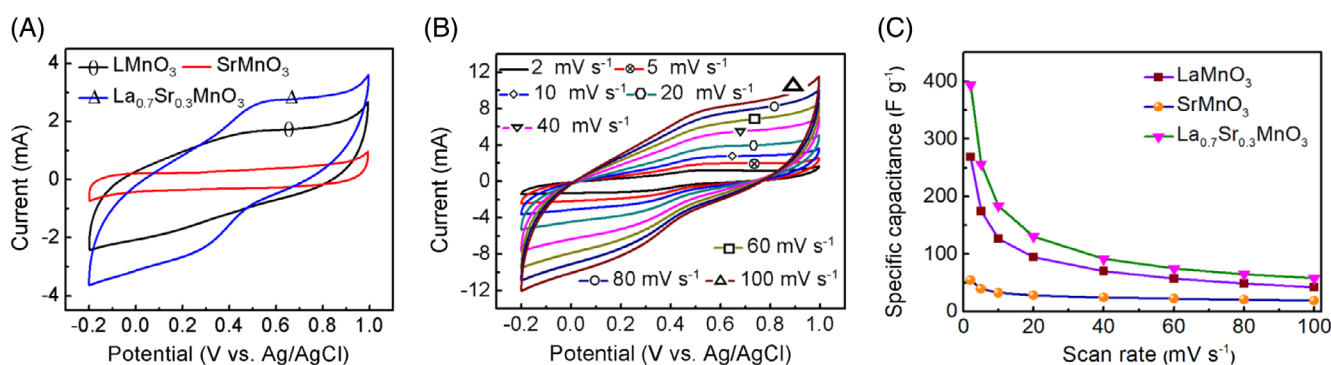
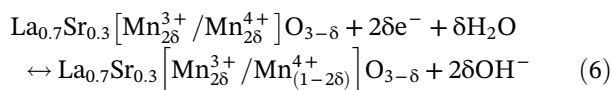


**FIGURE 3** A, CV curve of  $\text{LaMnO}_3$ ,  $\text{SrMnO}_3$ , and  $\text{La}_{0.7}\text{Sr}_{0.3}\text{MnO}_3$  electrode at fixed scan rate  $10 \text{ mV s}^{-1}$ . B, CV curves at all scan rates for  $\text{La}_{0.7}\text{Sr}_{0.3}\text{MnO}_3$  electrode. C, Specific capacitance vs scan rates for all three samples [Colour figure can be viewed at [wileyonlinelibrary.com](http://wileyonlinelibrary.com)]

active sites, resulting in greater specific capacitance. At higher scan rates, the electrolyte ions get lesser interaction time which effectively decreases the specific capacitance. In the CV curves of  $\text{La}_{0.7}\text{Sr}_{0.3}\text{MnO}_3$ , there is a redox peak around 0.55 V (vs Ag/AgCl), which corresponds to the transition  $\text{Mn}^{3+} \leftrightarrow \text{Mn}^{4+}$ .<sup>16</sup> The charge imbalance developed in  $\text{LaMnO}_3$  lattice due to the substitution of  $\text{La}^{3+}$  ions by  $\text{Sr}^{2+}$  ions is compensated either by oxidizing the  $\text{Mn}^{3+}$  ions to  $\text{Mn}^{4+}$  or by introducing oxygen vacancies. In both alkaline and neutral electrolytes, intercalation of ions with active sites plays the main role in charge storage. The redox reaction occurs in the present case can be expressed as<sup>19</sup>:



Therefore, more oxygen vacancies are formed in the lattice, there would be more room for  $\text{OH}^-$  ions to fill. This results in greater charge storage. Thus, it is confirmed that the pseudocapacitive mechanism plays the main role in charge storage. The charging and discharging curves are symmetric to each other, which reflect excellent redox reversibility and outstanding supercapacitive behavior of  $\text{La}_{0.7}\text{Sr}_{0.3}\text{MnO}_3$  electrode. The underlying charge storage mechanisms of  $\text{La}_{0.7}\text{Sr}_{0.3}\text{MnO}_3$  can be estimated using the power law. According to this law, the anodic peak current ( $I_p$ ) increases with scan rates ( $\nu$ ). This law can be expressed as  $I_p = a\nu^b$ , where, both  $a$  and  $b$  are adjustable parameters, and the role of  $b$  is important to determine the storage mechanism.<sup>38,42,43</sup>  $b = 0.5$  implies that the storage mechanism is controlled via faradic redox reaction, whereas  $b = 1$  indicates that the charge storage occurs via

Double-layer formation. The slope of  $\log I_p$  vs  $\log \nu$  plot (Figure 4A) corresponds to the value of  $b$ . For  $\text{La}_{0.7}\text{Sr}_{0.3}\text{MnO}_3$ , the value of  $b$  is 0.48, which indicates the charge storage in the sample is dominated by the redox process. This result indicates that the peak current varies linearly with the square roots of scan rate in agreement with the graph obtained from the experimental data (Figure 4B). Thus, the faradaic redox process plays dominating role in charge storage. The charge storage mechanisms can be quantitatively evaluated by the method suggested by Dunn.<sup>43</sup> According to this method, the current at any particular potential is the sum of the contribution from the capacitive part ( $\propto \nu$ ) as well as the contribution of the faradic reaction ( $\propto \nu^{1/2}$ ). This can be expressed by Equation (7).

$$i(V) = k_1\nu + k_2\nu^{1/2} \quad (7)$$

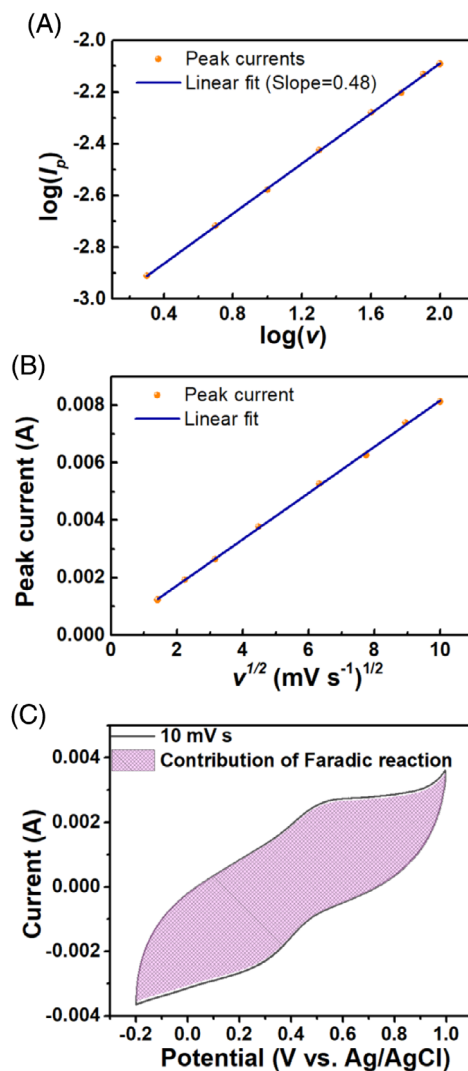


**FIGURE 4** A, Plots for power law method; B, variation of peak current with the square root of scan rates; and C, CV curve of  $\text{La}_{0.7}\text{Sr}_{0.3}\text{MnO}_3$  at a scan rate of  $10 \text{ mV s}^{-1}$  showing the redox contribution due to Dunn [Colour figure can be viewed at [wileyonlinelibrary.com](http://wileyonlinelibrary.com)]

The CV curve of  $\text{La}_{0.7}\text{Sr}_{0.3}\text{MnO}_3$  reveals that 97.5% of the total capacity is controlled by faradaic charge storage process (Figure 4C). This means that the charge storage of  $\text{La}_{0.7}\text{Sr}_{0.3}\text{MnO}_3$  composite is fully controlled by the faradaic redox process rather than capacitive process.

The charge storage behavior of  $\text{La}_{0.7}\text{Sr}_{0.3}\text{MnO}_3$  electrode can be further understood following the method introduced by Trasatti.<sup>44</sup> According to Trasatti, the total specific capacitance ( $C_{\text{total}}$ ) is the sum of the specific capacitances of the inner part ( $C_{\text{in}}$ ) and the outer part ( $C_{\text{out}}$ ) of the electrode, that is,  $C_{\text{total}} = C_{\text{in}} + C_{\text{out}}$ .<sup>44-46</sup> The inner part comes from the bulk of the material which is

due to the redox reactions. On the other hand,  $C_{\text{out}}$  arises from the capacitive process. The total specific capacitance, that is,  $C_{\text{total}}$  can be obtained if we allow adequate time to interact the electrolyte ions with the electrode, which can be estimated from the  $C_{\text{sp}}$  vs  $v^{1/2}$  curve upto  $v \rightarrow 0$  (Figure 5A). The estimated  $C_{\text{total}}$  was  $473.4 \text{ F g}^{-1}$ , which is the highest possible specific capacitance  $\text{La}_{0.7}\text{Sr}_{0.3}\text{MnO}_3$  can attain. Subsequently,  $C_{\text{out}}$  could be estimated by extrapolating the  $C_{\text{sp}}$  vs  $v^{-1/2}$  curve upto  $v^{-1/2} \rightarrow 0$ , that is, the scan rate tends to very high value (Figure 5B). For the extrapolation of the curves, we used the low scan rate ( $2^{-20} \text{ mVs}^{-1}$ ) data only, since at higher scan rates, these curves deviate from linear behavior. The deviation arises from the ohmic drop and irreversible redox process. For  $\text{La}_{0.7}\text{Sr}_{0.3}\text{MnO}_3$ , the highest possible surface contribution to the specific capacitance was estimated to be approximately  $11.7 \text{ F g}^{-1}$ , while the rest, that is,  $461.7 \text{ F g}^{-1}$  is due to the redox controlled process. This study also agrees with the Dunn method which reveals that the redox process is the key player for charge storage.

Electrochemical performance of  $\text{La}_{0.7}\text{Sr}_{0.3}\text{MnO}_3$  could be further investigated by performing GCD at different current densities between 1 and  $10 \text{ A g}^{-1}$ , within the same potential range ( $-0.2\text{--}1 \text{ V}$ ) in  $1 \text{ M Na}_2\text{SO}_4$

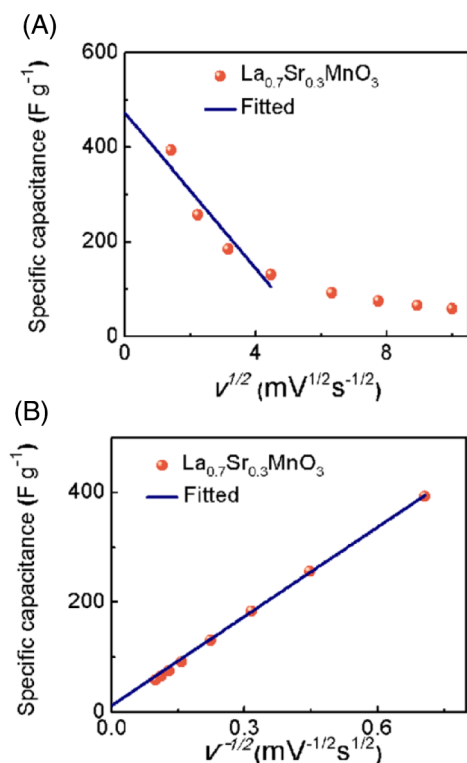


**FIGURE 5** A, Plot of specific capacitance vs  $v^{1/2}$  and B, variation of specific capacitance vs  $v^{-1/2}$  for  $\text{La}_{0.7}\text{Sr}_{0.3}\text{MnO}_3$  [Colour figure can be viewed at [wileyonlinelibrary.com](http://wileyonlinelibrary.com)]

electrolyte. Figure 6A presents the comparative GCD plots of all three samples at a particular current density of  $1 \text{ A g}^{-1}$ . As can be noticed, for a particular current density, the  $\text{La}_{0.7}\text{Sr}_{0.3}\text{MnO}_3$  electrode takes longer time for charging and discharging, which ensures a higher charge capacity of the electrode. On the other hand, the discharge curves of  $\text{LaMnO}_3$  and  $\text{La}_{0.7}\text{Sr}_{0.3}\text{MnO}_3$  are deviated from linearity, indicating the contribution of redox-dominated storage process in these electrodes. This observation is also in full agreement with that obtained from CV data. The GCD plots of  $\text{La}_{0.7}\text{Sr}_{0.3}\text{MnO}_3$  at different current densities are shown in Figure 6B. The highest specific capacitance offered by  $\text{La}_{0.7}\text{Sr}_{0.3}\text{MnO}_3$  was  $409.4 \text{ F g}^{-1}$  at the lowest current density ( $1 \text{ A g}^{-1}$ ), which decreases for higher current densities. The material exhibits high rate capability due to its excellent charge reversibility. On the other hand, the highest specific capacitance values offered by  $\text{LaMnO}_3$  and  $\text{SrMnO}_3$  at the lowest current density ( $1 \text{ A g}^{-1}$ ) were  $256.6$  and  $45.7 \text{ F g}^{-1}$ , respectively (GCD plots of these two materials are shown in Figure S2A, B of the supplementary information).

Performances of the electrode materials have also been investigated by EIS, which is a nondestructive process, providing important kinetic information about the electrode materials. The data have been recorded in the  $0.01 \text{ Hz--}100 \text{ kHz}$  frequency range, applying a small perturbation voltage of  $10 \text{ mV}$ . The EIS results of the samples are presented in Figure 6C in the form of Nyquist plots. In the high-frequency region, a small semi-circular loop appeared at the beginning of the curve (inset of Figure 6C). This semi-circular loop arises due to small series resistance ( $R_s$ ) and a parallel combination of charge transfer resistance ( $R_{\text{ct}}$ ) and constant phase element (CPE). From the EIS curves, it is clear that the  $\text{La}_{0.7}\text{Sr}_{0.3}\text{MnO}_3$  sample has relatively low  $Z'$  and  $Z''$  compared to other two samples. The EIS plot of  $\text{La}_{0.7}\text{Sr}_{0.3}\text{MnO}_3$  was fitted with Z-view software and presented in Figure 6D. Corresponding equivalent circuit is represented as an inset of Figure 6D. The Bode magnitude plot ( $|Z|$  vs  $\log f$ ) of  $\text{La}_{0.7}\text{Sr}_{0.3}\text{MnO}_3$  (not shown) was used to calculate the contribution of specific capacitance due to double-layer formation by using  $|Z| = 1/C_{\text{dl}}$  (at  $\omega = 1$ ) relation.<sup>47</sup> The  $C_{\text{dl}}$  value obtained from the plot was  $37.24 \text{ F g}^{-1}$ , which agrees well with the value predicted from Trasatti plot. We could calculate the low-frequency specific capacitance of the electrode material ( $\text{La}_{0.7}\text{Sr}_{0.3}\text{MnO}_3$ ) using the relation  $C_{\text{sp}} = \frac{1}{(2\pi f Z_{\text{im}})}$ , where  $Z_{\text{im}}$  refers to the imaginary impedance at lowest frequency.<sup>47,48</sup> The estimated  $C_{\text{sp}}$  value was  $298.67 \text{ F g}^{-1}$ , which is lower than the values estimated from CV or GCD analysis of the sample. High electrolyte ion density and high ion transfer resistance of the solution result in



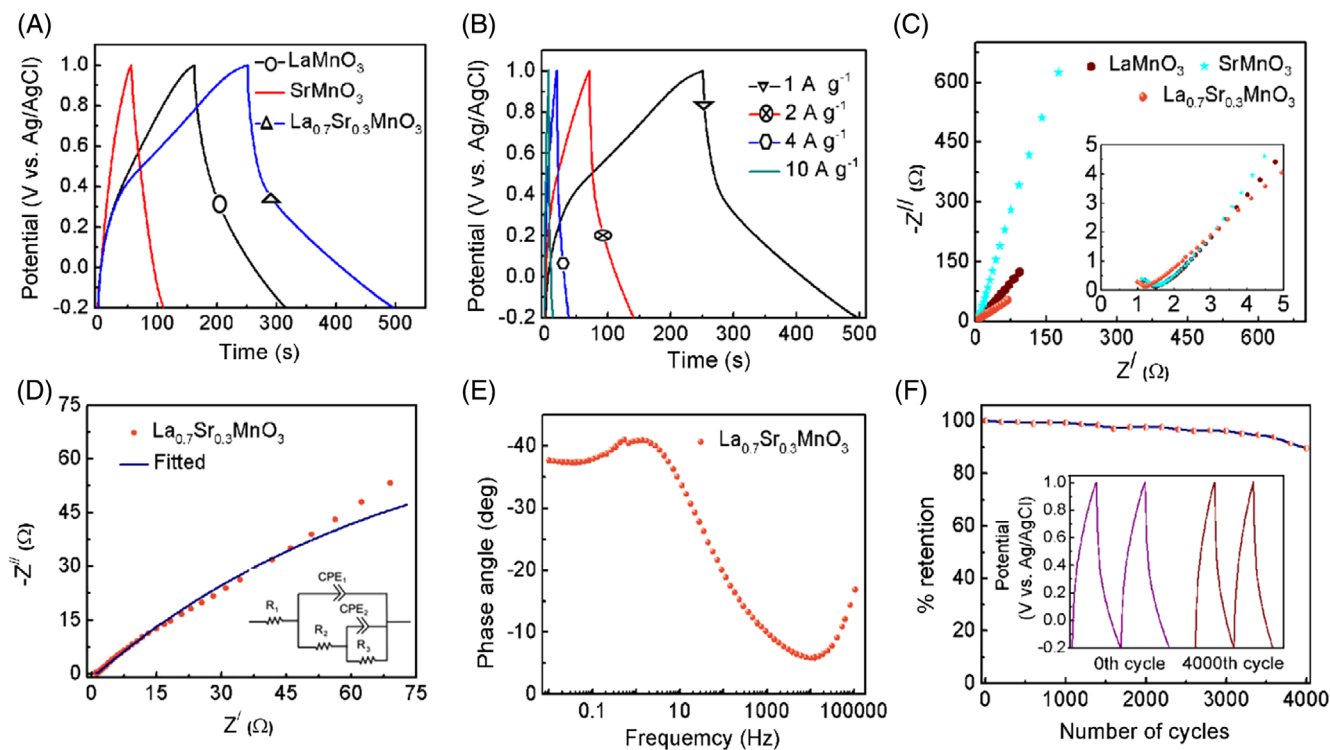


**FIGURE 6** A, GCD curves of  $\text{LaMnO}_3$ ,  $\text{SrMnO}_3$ , and  $\text{La}_{0.7}\text{Sr}_{0.3}\text{MnO}_3$  at current density  $1 \text{ A g}^{-1}$ ; B, GCD curves of  $\text{La}_{0.7}\text{Sr}_{0.3}\text{MnO}_3$  at different current densities; C, Nyquist plots of all three samples in  $1 \text{ M Na}_2\text{SO}_4$  electrolyte (*inset*) in high-frequency region; D, EIS plot of  $\text{La}_{0.7}\text{Sr}_{0.3}\text{MnO}_3$  along with fitted curve and (*inset*) equivalent circuit; E, Bode phase plot for  $\text{La}_{0.7}\text{Sr}_{0.3}\text{MnO}_3$  sample; and F, cyclic stability study of  $\text{La}_{0.7}\text{Sr}_{0.3}\text{MnO}_3$  sample, (*inset*) GCD curves during 1st and 4000th cycle [Colour figure can be viewed at [wileyonlinelibrary.com](http://wileyonlinelibrary.com)]

the decrease of specific capacitance.<sup>48</sup> From the Bode phase plot of  $\text{La}_{0.7}\text{Sr}_{0.3}\text{MnO}_3$  presented in Figure 6E, it is possible to predict the charge storage mechanism in the device. For EDLC-type materials, the phase angle at low frequency, that is,  $0.01 \text{ Hz}$ , reaches to  $90^\circ$ , whereas, for pseudocapacitive materials the phase angle is  $37.7^\circ$ , which is much less than  $90^\circ$ . The low phase angle of  $\text{La}_{0.7}\text{Sr}_{0.3}\text{MnO}_3$  indicates the pseudocapacitance mechanism is predominant in the charge storage process of the electrode.

Cyclic stability of the electrode material was studied by recording the GCD cycles of the working electrode over 4000 cycles at a fixed current density of  $10 \text{ A g}^{-1}$ . As can be seen in the retention vs cycle number plots presented in Figure 6F, the material retains about 89.6% of specific capacitance even after 4000 charge–discharge cycles. The nature of charge–discharge cycle remained almost same after 4000 GCD cycles, although there is a slight decrease in charging and discharging time. The 1st and 4000th GCD cycles are shown in the inset of the Figure. The material retains a Coulombic efficiency of 86% after 4000 charge–discharge cycles. This excellent long-term stability of the material along with excellent Coulombic efficiency demonstrates the

nanostructured  $\text{La}_{0.7}\text{Sr}_{0.3}\text{MnO}_3$  is an efficient electrode material for supercapacitors. To further explore the supercapacitive performance of the  $\text{La}_{0.7}\text{Sr}_{0.3}\text{MnO}_3$  sample, a prototype ASC device was fabricated (schematic diagram and prototype ASC are shown in Figure 7A). Electrochemical performances of the device were tested by studying all three conventional electrochemical techniques, that is, CV, GCD, and EIS. The CV traces were recorded in a large potential window of  $1.8 \text{ V}$  ( $0\text{--}1.8 \text{ V}$ ). The CV plots of  $\text{La}_{0.7}\text{Sr}_{0.3}\text{MnO}_3//\text{AC}$  ASC at various scan rates are presented in Figure 7B. The ASC exhibited undistorted CV curves even at elevated scan rates, which suggests an excellent reversibility. There was no indication of gas evolution from the electrode. The ASC exhibited a maximum specific capacitance of  $192.6 \text{ F g}^{-1}$  at the lowest scan rate of  $2 \text{ mV s}^{-1}$ . GCD study of the ASC was also performed for current densities between 1 and  $10 \text{ A g}^{-1}$  (Figure 7C). The specific capacitance decreased from 197 to  $125.6 \text{ F g}^{-1}$  with the increase of current density from 1 to  $10 \text{ A g}^{-1}$ , which suggests an outstanding rate capability of the  $\text{La}_{0.7}\text{Sr}_{0.3}\text{MnO}_3//\text{AC}$  ASC. At the same time, the Coulombic efficiency increased from 85.15% to 90.4%, indicating a rapid intercalation/deintercalation of

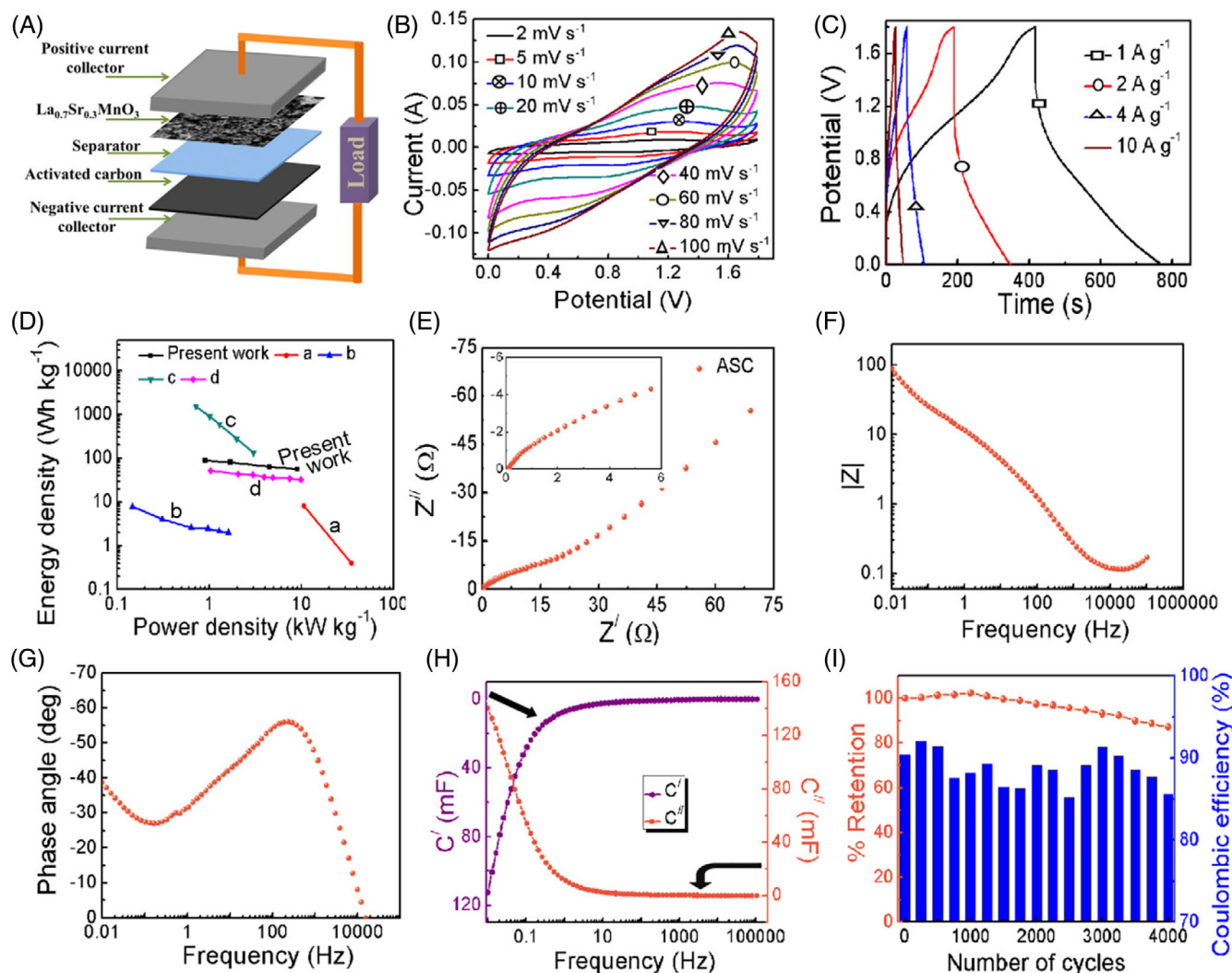


**FIGURE 7** A, Schematic of prototype of  $\text{La}_{0.7}\text{Sr}_{0.3}\text{MnO}_3//\text{AC}$  ASC; B, CV plots of ASC at different scan rates; C, GCD plots at different current densities within the same window; D, Ragone plot [a-,<sup>52</sup> b-,<sup>15</sup> c-,<sup>53</sup> d-<sup>54</sup>]; E, Nyquist plot of impedance, (*inset*) high-frequency region; F, Bode magnitude plots; G, Bode phase plots; H, real and imaginary component of capacitance vs frequency plot; and I, long term stability plot for 4000 cycles, (*inset*) Coulombic efficiency plots for 4000 cycles [Colour figure can be viewed at [wileyonlinelibrary.com](http://wileyonlinelibrary.com)]

**TABLE 1** Various parameters of  $\text{La}_{0.7}\text{Sr}_{0.3}\text{MnO}_3//\text{AC}$  ASC

Current density ( $\text{A g}^{-1}$ )	Charge time (s)	Discharge time (s)	Specific capacitance ( $\text{F g}^{-1}$ )	Coulombic efficiency (%)	Specific energy ( $\text{Wh kg}^{-1}$ )	Specific power ( $\text{kW kg}^{-1}$ )
1	416.4	354.6	197	85.2	88.7	0.9
2	189.6	162.8	180.9	85.9	81.2	1.7
4	57.6	50.8	141.1	88.2	63.5	4.5
10	25.0	22.6	125.6	90.4	56.5	9.0

electrolyte ions into the electrochemically active sites. The  $\text{La}_{0.7}\text{Sr}_{0.3}\text{MnO}_3//\text{AC}$  ASC exhibited a highest specific energy of  $88.7 \text{ Wh kg}^{-1}$  at a power density of  $0.9 \text{ kW kg}^{-1}$  and  $56.5 \text{ Wh kg}^{-1}$  at a higher power density of  $9 \text{ kW kg}^{-1}$

(Table 1). The Ragone plot of the  $\text{La}_{0.7}\text{Sr}_{0.3}\text{MnO}_3//\text{AC}$  ASC along with some other reported results is shown in Figure 7D. As can be seen, the  $\text{La}_{0.7}\text{Sr}_{0.3}\text{MnO}_3//\text{AC}$  ASC has moderate energy and power densities. The energy

efficiency of the ASC has also been calculated using the relation<sup>49</sup>:

$$\text{Energy efficiency (\%)} = \frac{\text{energy density}_{(\text{discharge})}}{\text{energy density}_{(\text{charge})}} \times 100(\%) \quad (8)$$

The energy efficiency of the supercapacitor was approximately 90% at current density 10 A g<sup>-1</sup>, and it reduces to 85% for a current density of 1 A g<sup>-1</sup>.

The Nyquist plot of the ASC is shown in Figure 7E. From the high-frequency region (inset of Figure 7E), it is clear that there is almost zero or negligible series resistance and relatively low charge transfer resistance (~7 Ω). At the low-frequency region, the curve is inclined to the x-axis with an angle of approximately 45°, which suggests the presence of diffusion-controlled Warburg element. The EIS data were further utilized to characterize the device. Typical Bode magnitude and Bode phase plots of La<sub>0.7</sub>Sr<sub>0.3</sub>MnO<sub>3</sub>//AC ASC are shown in Figure 7F, G. At a lower frequency such as 0.01 Hz, the phase angle reached to -38.3°, clearly suggesting the pseudocapacitive nature of the device. On the other hand, the figure of merit of a supercapacitor can be estimated from its relaxation time. The relaxation time was calculated using the equivalence  $\tau_0 = \frac{1}{2\pi f_0}$ , where,  $f_0$  is the frequency at the phase angle -45° (where the contribution of capacitive and resistive impedance are identical).<sup>50</sup> The time constant obtained from the Bode phase plot was 8.7 ms. This small value of the time constant facilitates quick ion transport during the electrochemical process.

The variation of real ( $C'$ ) and imaginary ( $C''$ ) components of the La<sub>0.7</sub>Sr<sub>0.3</sub>MnO<sub>3</sub>//AC ASC device with frequency was estimated and shown in Figure 7H. The real part of capacitance depends on the nature of electrolyte, porosity, and the active mass of electrode material. However, the imaginary component is directly related to energy dissipation.<sup>51</sup> From the curves, it is clear that the resistive behavior of La<sub>0.7</sub>Sr<sub>0.3</sub>MnO<sub>3</sub> at the high-frequency region changes to capacitive at lower frequencies due to ion migration. The long-term stability of the La<sub>0.7</sub>Sr<sub>0.3</sub>MnO<sub>3</sub>//AC ASC was further investigated by performing 4000 GCD cycles at a fixed current density of 10 A g<sup>-1</sup> (Figure 7i). As can be noticed, about 87.2% of the specific capacitance retained even after 4000 GCD cycles, suggesting excellent stability of the device. The Coulombic efficiency of the La<sub>0.7</sub>Sr<sub>0.3</sub>MnO<sub>3</sub>//AC ASC device was also measured over 4000 cycles, which varied in-between 90.4% and 85.6%. The results obtained in the present study suggest that nanostructured La<sub>0.7</sub>Sr<sub>0.3</sub>MnO<sub>3</sub> is an excellent electrode material for supercapacitor applications.


## 4 | CONCLUSIONS

In summary, we demonstrated the possibility of synthesizing strontium (Sr)-doped LaMnO<sub>3</sub> (La<sub>0.7</sub>Sr<sub>0.3</sub>MnO<sub>3</sub>) perovskite nanostructures through ball-milling assisted solid-state reaction. XRD study confirmed the ABO<sub>3</sub>-type rhombohedral structure of La<sub>0.7</sub>Sr<sub>0.3</sub>MnO<sub>3</sub>. N<sub>2</sub> adsorption-desorption study confirmed the mesoporous texture of the nanostructures. Electrochemical performances of the La<sub>0.7</sub>Sr<sub>0.3</sub>MnO<sub>3</sub> nanostructures studied in neutral aqueous electrolyte (1 M Na<sub>2</sub>SO<sub>4</sub>) revealed a maximum specific capacitance of 393.5 F g<sup>-1</sup>. Pseudocapacitive mechanism was seen to be responsible for charge storage in the material. Furthermore, the material has been utilized to fabricate asymmetric La<sub>0.7</sub>Sr<sub>0.3</sub>MnO<sub>3</sub>//AC supercapacitors with the same neutral electrolyte. Asymmetric supercapacitors made of La<sub>0.7</sub>Sr<sub>0.3</sub>MnO<sub>3</sub> nanostructures as active electrode material operated within a potential window of 1.8 V and exhibited a highest specific capacitance of 197 F g<sup>-1</sup>. Incorporation of Sr in LaMnO<sub>3</sub> nanostructures was seen to improve their electrochemical performance as well as their electrochemical stability. The results presented in this work clearly indicate that Sr-doped lanthanum magnetite perovskite nanostructures can be used as electrode material for fabricating supercapacitors with high energy density.

## ACKNOWLEDGEMENTS

U.P. acknowledges CONACyT, Mexico for financial support (Grant # CB-A1-S-26720). S.D. is thankful to Jadavpur University for financial support through RUSA 2.0 (Ref No. R-11/281/19) research grant and Science and Engineering Research Board, Department of Science and Technology, Government of India for financial support through the "Core Research Grant" (File no #CRG/2019/001575). S.S. is thankful to CSIR, Govt. of India for financial support (File No.-09/096 (0898)/2017-EMR-I).

## ORCID

Francisco Enrique Cancino-Gordillo  <https://orcid.org/0000-0001-8286-5734>

Sachindranath Das  <https://orcid.org/0000-0002-6938-6701>

## REFERENCES

- Chodankar NR, Dubal DP, Ji SH, Kim DH. Self-assembled nickel pyrophosphate-decorated amorphous bimetal hydroxides 2D-on-2D nanostructure for high-energy solid-state asymmetric supercapacitor. *Small*. 2019;15:1.
- Dubal DP, Chodankar NR, Kim DH, Gomez-Romero P. Towards flexible solid-state supercapacitors for smart and wearable electronics. *Chem Soc Rev*. 2018;47:2065-2129.

- Borenstein A, Hanna O, Attias R, Luski S, Brousse T, Aurbach D. Carbon-based composite materials for supercapacitor electrodes: a review. *J Mater Chem A*. 2017;5:12653-12672.
- Tsai IL, Cao J, Le Fevre L, et al. Graphene-enhanced electrodes for scalable supercapacitors. *Electrochim Acta*. 2017;257:372-379.
- Ramli NIT, Abdul Rashid S, Sulaiman Y, et al. Physicochemical and electrochemical properties of carbon nanotube/graphite nanofiber hybrid nanocomposites for supercapacitor. *Sources*. 2016;328:195-202.
- Siddique AH, Butt R, Bokhari SW, Raj DV, Zhou X, Liu Z. All graphene electrode for high-performance asymmetric supercapacitor. *Int J Energy Res*. 2020;44:1244-1255.
- Xia H, Shirley Meng Y, Yuan G, Cui C, Lu L. A symmetric RuO<sub>2</sub>/RuO<sub>2</sub> supercapacitor operating at 1.6 V by using a neutral aqueous electrolyte. *Electrochem Solid St*. 2012;15:A60.
- Iro ZS, Subramani C, Dash SS. A brief review on electrode materials for supercapacitor. *Int J Electrochem Sci*. 2016;11:10628.
- Ray A, Roy A, Saha S, et al. Electrochemical energy storage properties of Ni-Mn-oxide electrodes for advance asymmetric supercapacitor application. *Langmuir*. 2019;acs.langmuir.9b00955.
- Roy A, Ray A, Sadhukhan P, Saha S, Das S. Morphological behaviour, electronic bond formation and electrochemical performance study of V<sub>2</sub>O<sub>5</sub>-polyaniline composite and its application in asymmetric supercapacitor. *Mater Res Bull*. 2018;107:379-390.
- Majumdar D, Maiyalagan T, Jiang Z. Recent Progress in ruthenium oxide-based composites for supercapacitor applications. *ChemElectroChem*. 2019;6:4343-4372.
- Zhu H, Liu J, Zhang Q, Wei J. High electrochemical performance of metal azolate framework-derived ZnO/Co<sub>3</sub>O<sub>4</sub> for supercapacitors. *Int J Energy Res*. 2020;44:8654-8665.
- Chodankar NR, Rama Raju GS, Park B, et al. Potentiodynamic polarization assisted phosphorus-containing amorphous trimetal hydroxide nanofibers for highly efficient hybrid supercapacitors. *J Mater Chem A*. 2020;8:5721-5733.
- Chodankar NR, Patil SJ, Rama Raju GS, et al. Two-dimensional materials for high-energy solid-state asymmetric pseudocapacitors with high mass loadings. *ChemSusChem*. 2020;13:1582-1592.
- Mo H, Nan H, Lang X, et al. Influence of calcium doping on performance of LaMnO<sub>3</sub> supercapacitors. *Ceram Int*. 2018;44:9733-9741.
- Cao Y, Lin B, Sun Y, Yang H, Zhang X. Synthesis, structure and electrochemical properties of lanthanum manganese nanofibers doped with Sr and Cu. *J Alloys Compd*. 2015;638:204-213.
- Lu F, Xia T, Li Q, Wang J, Huo L, Zhao H. Heterostructured simple perovskite nanorod-decorated double perovskite cathode for solid oxide fuel cells: highly catalytic activity, stability and CO<sub>2</sub>-durability for oxygen reduction reaction. *Appl Catal Environ*. 2019;249:19-31.
- Sharma AP, Pradhan DK, Xiao B, Pradhan SK, Bahoura M. Lead-free epitaxial ferroelectric heterostructures for energy storage applications. *AIP Adv*. 2018;8:125112.
- Alexander CT, Mefford JT, Saunders J, Forslund RP, Johnston KP, Stevenson KJ. Anion-based pseudocapacitance of the perovskite library La<sub>1-x</sub>Sr<sub>x</sub>BO<sub>3-δ</sub> (B = Fe, Mn, Co). *ACS Appl Mater Interfaces*. 2019;11:5084-5094.
- Mefford JT, Hardin WG, Dai S, Johnston KP, Stevenson KJ. Anion charge storage through oxygen intercalation in LaMnO<sub>3</sub> perovskite pseudocapacitor electrodes. *Nat Mater*. 2014;13:726-732.
- Ruiz-Gonzalez L, Cortes-Gil R, Alonso JM, Gonzalez-Calbet JM, Vallet-Regi M. Revisiting the role of vacancies in manganese related perovskites. *Open Inorg Chem J*. 2007;1:37-46.
- Laiho R, Lisunov KG, Lähderanta E, et al. Low-field magnetic properties of LaMnO<sub>3+δ</sub> with 0.065 ≤ δ ≤ 0.154. *J Phys Chem Solid*. 2003;64:2313-2319.
- Cortés-Gil R, Arroyo A, Ruiz-González L, et al. Evolution of magnetic behaviour in oxygen deficient LaMnO<sub>3-δ</sub>. *J Phys Chem Solid*. 2006;67:579-582.
- Wang XW, Zhu QQ, Wang XE, Zhang HC, Zhang JJ, Wang LF. Structural and electrochemical properties of La<sub>0.85</sub>Sr<sub>0.15</sub>MnO<sub>3</sub> powder as an electrode material for supercapacitor. *J Alloys Compd*. 2016;675:195-200.
- Zhong C, Deng Y, Hu W, Qiao J, Zhang L, Zhang J. A review of electrolyte materials and compositions for electrochemical supercapacitors. *Chem. Soc. Rev*. 2015;44:7484-7539.
- Ramachandran R, Wang F. Electrochemical capacitor performance: Influence of Aqueous Electrolytes. *Supercapacitors - theoretical and practical solutions*. IntechOpen; 2016:51-68.
- Wang G, Zhang L, Zhang J. A review of electrode materials for electrochemical supercapacitors. *Chem Soc Rev*. 2012;41:797-828.
- Wang F, Xiao S, Hou Y, Hu C, Liu L, Wu Y. Electrode materials for aqueous asymmetric supercapacitors. *RSC Adv*. 2013;3:13059.
- Liu Y, Dinh J, Tade MO, Shao Z. Design of perovskite oxides as anion-intercalation-type electrodes for supercapacitors: cation leaching effect. *ACS Appl Mater Interfaces*. 2016;8:23774-23783.
- Guo J, Ma Y, Zhao K, et al. High-performance and ultra-stable aqueous supercapacitors based on a green and low-cost water-in-salt electrolyte. *ChemElectroChem*. 2019;6:5433-5438.
- Nforna EA. Structure and magnetic properties of lanthanum strontium ferrites nanopowders synthesized by thermal decomposition of mixed metal acetyl acetonates. *Int J Eng Res Technol*. 2015;4:907.
- Ray A, Roy A, Ghosh M, et al. Study on charge storage mechanism in working electrodes fabricated by sol-gel derived spinel NiMn<sub>2</sub>O<sub>4</sub> nanoparticles for supercapacitor application. *Appl Surf Sci*. 2019;463:513-525.
- Ma Z, Shao G, Fan Y, Wang G, Song J, Shen D. Construction of hierarchical α-MnO<sub>2</sub>Nanowires@ultrathin δ-MnO<sub>2</sub> nanosheets core-shell nanostructure with excellent cycling stability for high-Power asymmetric supercapacitor electrodes. *ACS Appl Mater Interfaces*. 2016;8:9050-9058.
- Saha S, Maji P, Pethsangave DA, et al. Effect of morphological ordering on the electrochemical performance of MnO<sub>2</sub>-graphene oxide composite. *Electrochim Acta*. 2019;317:199-210.
- Yang P, Qu X, Liu K, et al. Electrokinetic supercapacitor for simultaneous harvesting and storage of mechanical energy. *ACS Appl Mater Interfaces*. 2018;10:8010-8015.

36. Roy A, Ray A, Saha S, et al. NiO-CNT composite for high performance supercapacitor electrode and oxygen evolution reaction. *Electrochim Acta*. 2018;283:327-337.
37. Toby BH, Von Dreele RB. GSAS-II: the genesis of a modern open-source all purpose crystallography software package. *J Appl Cryst*. 2013;46:544-549.
38. Roy A, Ray A, Saha S, Das S. Investigation on energy storage and conversion properties of multifunctional PANI-MWCNT composite. *Int J Hydrogen Energy*. 2018;43:7128-7139.
39. Inagaki S, Fukushima Y, Kuruda K. Synthesis of highly ordered mesoporous materials from a layered polysilicate. *J Chem Soc Chem Commun*. 1993;680.
40. Das T, Uyama H, Nandi M. Pd-bound functionalized mesoporous silica as active catalyst for Suzuki coupling reaction: effect of  $\text{OAc}^-$ ,  $\text{PPh}_3$  and  $\text{Cl}^-$  ligands on catalytic activity. *J Solid State Chem*. 2018;260:132-141.
41. Ortiz-Quiñonez JL, García-González L, Cancino-Gordillo FE, Pal U. Particle dispersion and lattice distortion induced magnetic behavior of  $\text{La}_{1-x}\text{Sr}_x\text{MnO}_3$  perovskite nanoparticles grown by salt-assisted solid-state synthesis. *Mater Chem Phys*. 2020;246.
42. Conway BE. Transition from “Supercapacitor” to “Battery” behavior in electrochemical energy storage. *J Electrochem Soc*. 1991;138:1539-1548.
43. Augustyn V, Simon P, Dunn B. Pseudocapacitive oxide materials for high-rate electrochemical energy storage. *Energy Environ Sci*. 2014;7:1597.
44. Ardizzone S, Fregonara G, Trasatti S. “Inner” and “outer” active surface of  $\text{RuO}_2$  electrodes. *Electrochim Acta*. 1990;35:263-267.
45. Sankar KV, Selvan RK. The preparation of  $\text{MnFe}_2\text{O}_4$  decorated flexible graphene wrapped with PANI and its electrochemical performances for hybrid supercapacitors. *RSC Adv*. 2014;4:17555.
46. Ray A, Roy A, Sadhukhan P, et al. Electrochemical properties of  $\text{TiO}_2$ - $\text{V}_2\text{O}_5$  nanocomposites as a high performance supercapacitors electrode material. *Appl Surf Sci*. 2018;443:581-591.
47. Bai M-H, Liu T-Y, Luan F, Li Y, Liu X-X. Electrodeposition of vanadium oxide-polyaniline composite nanowire electrodes for high energy density supercapacitors. *J Mater Chem A*. 2014;2:10882-10888.
48. Islam DA, Chakraborty A, Roy A, Das S, Acharya H. Fabrication of graphene-oxide (GO)-supported sheet-like  $\text{CuO}$  nanostructures derived from a metal-organic-framework template for high-performance hybrid supercapacitors. *ChemSel*. 2018;3:11816-11823.
49. Eftekhari A. Energy efficiency: a critically important but neglected factor in battery research. *Sustain Energy Fuels*. 2017;1:2053-2060.
50. Zhang J, Zhao XS. On the configuration of supercapacitors for maximizing electrochemical performance. *ChemSusChem*. 2012;5:818-841.
51. Portet C, Taberna PL, Simon P, Flahaut E, Power J. Influence of carbon nanotubes addition on carbon-carbon supercapacitor performances in organic electrolyte. *Sources*. 2005;139:371-378.
52. Cao Y, Lin B, Sun Y, Yang H, Zhang X. Symmetric/asymmetric supercapacitor based on the perovskite-type lanthanum cobaltate nanofibers with Sr-substitution. *Electrochim Acta*. 2015;178:398-406.
53. Lang X, Mo H, Hu X, Tian H. Supercapacitor performance of perovskite  $\text{La}_{1-x}\text{Sr}_x\text{MnO}_3$ . *Dalt Trans*. 2017;46:13720-13730.
54. Shafi PM, Joseph N, Thirumurugan A, Bose AC. Enhanced electrochemical performances of agglomeration-free  $\text{LaMnO}_3$  perovskite nanoparticles and achieving high energy and power densities with symmetric supercapacitor design. *Chem Eng J*. 2018;338:147-156.

## SUPPORTING INFORMATION

Additional supporting information may be found online in the Supporting Information section at the end of this article.

**How to cite this article:** Roy A, Cancino-Gordillo FE, Saha S, Pal U, Das S. Performance of asymmetric supercapacitor fabricated with perovskite-type  $\text{Sr}^{2+}$ -incorporated  $\text{LaMnO}_3$  ( $\text{La}_{0.7}\text{Sr}_{0.3}\text{MnO}_3$ ) nanostructures in neutral 1M  $\text{Na}_2\text{SO}_4$  aqueous electrolyte. *Int J Energy Res*. 2021; 1–13. <https://doi.org/10.1002/er.6727>